# Influence of the nozzle inner geometry on the particle history during cold spray process

Chrystelle A Bernard, Hidemasa Takana, O. Lame, Kazuhiro Ogawa, Cavaillé J.-Y.

**Influence of the nozzle inner geometry on the particle history during cold spray process**

C.A. Bernard[a,b,c], H. Takana[d], O. Lame[e], K. Ogawa[b,c], J.-Y. Cavaillé[b]

[a]Frontier Research Institute for Interdisciplinary Sciences, Tohoku University, Sendai, Japan
[b]ELyTMaX UMI3757, CNRS–Université de Lyon–Tohoku University, International Joint Unit, Tohoku University, Sendai, Japan
[c]Fracture and Reliability Research Institute, Tohoku University, Sendai, Japan
[d]Institute of Fluid Science, Tohoku University, Sendai, Japan
[e]Materials Engineering and Science (MATEIS), CNRS, INSA-Lyon, UMR5510, Université de Lyon, Villeurbanne, France

**Abstract**

High particle temperature and low particle velocity are required to successfully deposit polymer particles by cold spray process. To increase the particle temperature, a solution is to use a relatively long nozzle to increase the particle resident time inside the nozzle and limit the expansion of the supersonic flow. However, to do this, due to manufacturing limitations, several nozzles must be attached in series (until the desired length is reached), or alternatively, irregularities must be introduced into the inner shape of the nozzle. In this study, we aim to analyze the effect of 20% nozzle reduction of cross section area at the center of a 240 mm long nozzle using computational fluid dynamics (CFD). At the intersection between the two sections, several phenomena take place: (i) the flow chokes and (ii) particles rebound at the intersection leading them to go upstream. For particles with a diameter larger than 30 µm, 20 to 25% of the particles rebound inside the nozzle due to the larger influence of the inertia and the Saffman lift force. For these particles, larger temperature and lower velocity is recorded.

**Keywords**

Cold spray; fluid dynamics; polymer; long nozzle shape; deposition behavior; particle history; particle rebound

**Nomenclature**

In the text, subscript “p” or “g” is added to the given parameters to refer to either the particle or the gas, respectively. Parameters in **bold** refers to vectors. Openwork parameters, such as $\mathbb{d}$ for example, refers to 3×3 tensors. The $\langle\ \rangle$ symbol refers to the average value of the given parameter.

| | |
|---|---|
| $a_1, a_2, a_3$ | Model parameters associated to the drag coefficient |
| $A_p$ | Surface area of the particle (m$^2$) |
| $C_1$ | Model parameter dependent on $k$, $\varepsilon$ and S |
| $C_2$ | Model constant (= 1.9) |
| $C_{1\varepsilon}$ | Model constant (= 1.44) |
| $C_{3\varepsilon}$ | Model constant |
| $C_\mu$ | Model parameter |
| $C_D$ | Drag coefficient |
| $c_p$ | Heat capacity at constant pressure |
| $\mathbb{d}$ | Deformation tensor |
| $d_p$ | Particle diameter (m) |
| $D_{T,p}$ | Thermophoretic coefficient |
| $\boldsymbol{F}_{grav}$ | Force due to gravity (N) |

| | |
|---|---|
| $\boldsymbol{F}_{drag}$ | Force due to drag (N) |
| $\boldsymbol{F}_{lift}$ | Force due to Saffman lift (N) |
| $\boldsymbol{F}_{therm}$ | Force due to thermophoresis (N) |
| $\boldsymbol{g}$ | Gravity (m $s^{-2}$) |
| $G_k$ | Generation of turbulence kinetic energy due to mean velocity gradients |
| $G_b$ | Generation of turbulence kinetic energy due to buoyancy |
| $h$ | Convective heat transfer coefficient (W $m^2$) |
| $\mathbb{I}$ | Identity tensor |
| $k$ | Turbulent kinetic energy |
| $K_n$ | Knudsen number |
| $K$ | Ratio of thermal conductivity (gas/particle) |
| $m_p$ | Particle mass (kg) |
| p | Gas pressure (Pa) |
| $Re$ | Reynolds number |
| $S$ | Strain rate magnitude |
| $t$ | Time (s) |
| $T$ | Absolute temperature (K) |
| $T_\infty$ | Gas local temperature (K) |
| $\boldsymbol{u}$ | Velocity (m $s^{-1}$) |
| $Y_{d_p}$ | Mass fraction of particles with a diameter greater than $d_p$ |
| $Y_M$ | Contribution of the fluctuation dilatation in compressible turbulence to the overall dissipation rate |
| $\varepsilon$ | Turbulent dissipation rate ($m^2$ $s^{-3}$) |
| $\mu_g$ | Dynamic viscosity (Pa s) |
| $\mu_t$ | Turbulent viscosity (N $m^2$) |
| $\nu$ | Kinematic viscosity ($m^2$ $s^{-1}$) |
| $\rho$ | Density (kg $m^{-3}$) |
| $\sigma_k$ | Prandtl number for $k$ (= 1.0) |
| $\sigma_\varepsilon$ | Prandtl number for $\varepsilon$ (= 1.2) |

## 1. Introduction

Cold spray process, discovered in the 1980's by Papyrin et al. (Ref 1), has been extensively studied since the last decades, especially for the formation of metallic coatings on metallic substrates. Since the last 10 years, interest in obtaining polymer coatings on metallic substrates raised to increase the corrosion resistance, wear resistance, and lifespan of structures. As a new way to manufacture polymer coating, cold spray exhibits interesting features such as low temperature operation (i.e. lower than melting temperature), fast process, the possibility to coat complex structures and to add functionalities to them (Ref 2,3). However, polymer coatings by cold spray are generally characterized by low deposition efficiency and weak adhesion strength. One of the difficulties of polymer coatings by cold spray lies in the highly sensitive mechanical behavior of polymers to strain rate and temperature.

Using computational fluid dynamics (CFD), Alhulaifi et al. (Ref 4) designed different nozzles to deposit polyethylene powder on aluminum substrates. They demonstrated that a rather long diverging nozzle with a diffuser at the end was beneficial to cold spray polymer powder. A long nozzle length limits the

length of the supersonic flows and allows increasing the resident time of the particles inside the nozzle, and therefore, their temperature, while the diffuser at the end reduces the gas velocity at the nozzle output and minimizes the shear stresses on the substrate. Thus, the sprayed particles are less likely to erode the deposited particles. Also using a long nozzle, Ravi et al. (Ref 5,6) added 4% of fumed nano-alumina to the polymer feedstock to increase the deposition efficiency of ultra-high molecular weight polyethylene (UHMWPE). Even though 4 mm coating was obtained, the deposition efficiency remains lower than 1% and the coating exhibits porous microstructure. By analyzing the thermal properties of the raw powder, the rebounded particles, and the deposited particles, they demonstrated the change of crystallinity, and therefore, nano-microstructure of the deposited particles (Ref 6). This change of microstructure is due to the particle temperature increasing above its melting temperature. Recently, Khalkhali and collaborators (Ref 7,8) identified the deposition of several polymer particles on different polymer substrates. They showed that the critical velocity of polymer particles is highly dependent on the particle temperature. Thus, increasing the particle temperature allows expanding the deposition window at a given temperature. In addition, increasing the particle temperature allows decreasing the particle critical velocity.

Other authors investigated the deposition of polymer particles on metallic or polymer substrates. Xu and Hutchings (Ref 9) deposited polyolefin powder on polyethylene (PE) and aluminum substrates. If it was possible to manufacture a polyolefin coating on PE substrates at room temperature, its deposition on aluminum substrates was only possible after the formation of a thin melting layer of polymer on top of the metallic surface. Sulen and coworkers (Ref 2,3,10) developed superhydrophobic fluoropolymer coatings on stainless steel substrates. Recently, Sulen et al. (Ref 11) highly improved the deposition efficiency of fluoropolymer powders from less than 1% to around 60% by laser texturing the carbon steel substrates. Thus, strong mechanical interlocking occurs between the particles and the substrate.

To manufacture his long nozzle, Ravi et al. (Ref 5) attached together two 120 mm long diverging nozzles. Such system leads to the formation of a sharp step inside the nozzle leading to the flow to chokes once again inside the nozzle at the intersection between these two nozzles sections (Ref 5,12). In addition to disturb the flow field, the sharp step inside the nozzle might affect the particle trajectory and history inside the nozzle by rebounding on it. Thus, the objective of this study is to understand the effect of the step on the flow field and how this will affect the particle history and trajectory. Using computational fluid dynamics (CFD), we will investigate the possibility of particle rebound inside the nozzle and how the particle rebounding affects the particle temperature and velocity prior to the impact. In addition, comparison between the 120 mm × 2 long divergent nozzle and a conventional 240 mm long divergent nozzle will be carried out.

## 2. Modelling

### 2.1. Nozzle geometry

The nozzle investigated in this study has been developed by Ravi et al. (Ref 5) for the cold spray of ultra-high molecular weight polyethylene (UHMWPE). The system, reproduced schematically on Figure 1, consists in a converging-diverging section of 19 mm long, a 2.2 mm diameter powder feeding inlet, and two diverging straight nozzles of 120 mm long attached together by a connector. The standoff distance is set at 10 mm. The inlet and outlet diameters of the two 120 mm-long diverging are 4 mm and 5 mm, respectively. Such dimension for the nozzle inner shape induces a sharp reduction of 20% in the nozzle cross-section at the intersection between the two diverging nozzles. As previously shown using a 2D-axisymmetric modelling (Ref 12), at the intersection between the two diverging nozzles, the flow chokes due to the sharp change of section diameter leading to a second acceleration of the particles. In addition, because of the geometry irregularities in the nozzle inner shape, flow vortexes around the intersection as well as particles' rebound inside the nozzle can occur.

To better understand these phenomena, it is necessary to consider the particles' trajectories. Therefore, a 3D simulation with the presence of the particle inlet (see Figure 1) has been designed using ANSYS/FLUENT® 19.0. To capture the geometry discontinuity, bow shocks and expansion waves, a finer mesh was introduced near the nozzle's wall and substrate. It consists in a mesh refinement near the nozzle walls using 10 layers on the nozzle's wall and 5 layers on the substrate of cells parallel to the nozzle wall. The mesh consists of more than 10 millions quadrilateral elements.

The gas dynamics and particle history inside the nozzle of this new nozzle design are compared to a 240 mm long nozzle without nozzle section reduction. The inlet and outlet diameter of the 240 mm long nozzle are 4 mm and 5 mm, respectively. The boundary conditions are the same as the 120 mm × 2 long nozzle.

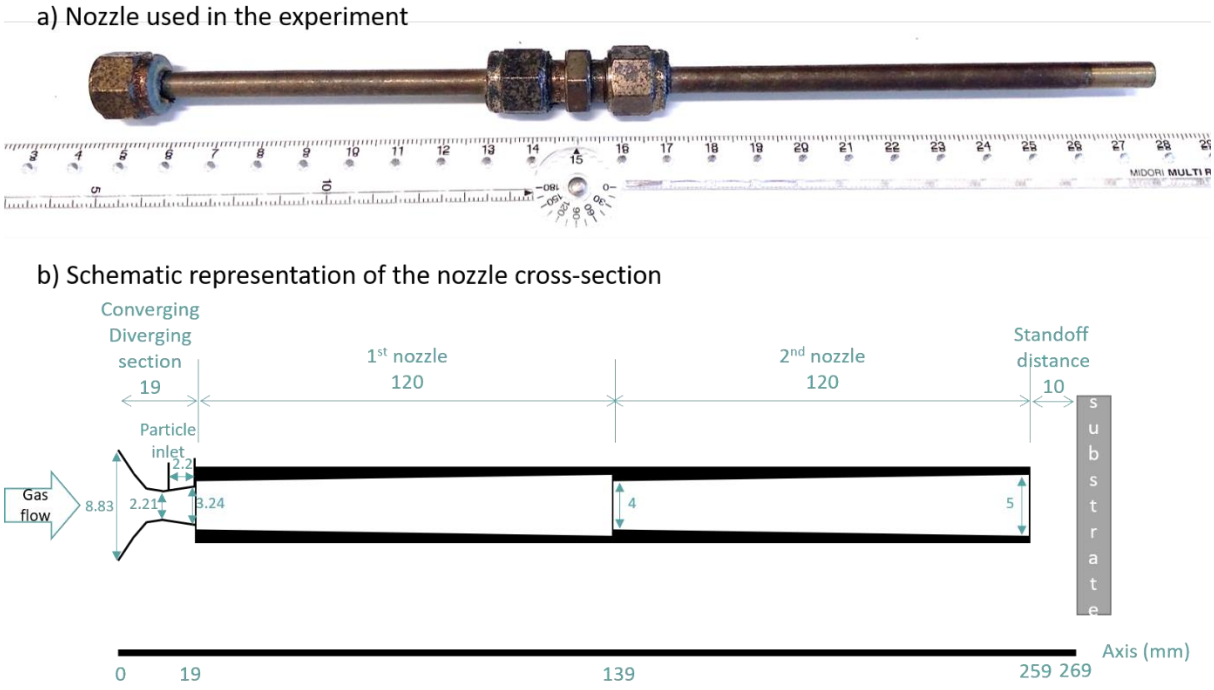


*Figure 1: a) Nozzle developed by Ravi et al. (Ref 5) and b) its schematic reproduction of the nozzle cross-section with the particle injection system. The nozzle assembly consists of two 120 mm divergent nozzles attached together. All dimensions are in mm.*

### 2.2. Particle-Laden gas flow modelling

To evaluate the gas flow field and the particles trajectories, the following assumptions are considered (Ref 13,14):

a) The flow is compressible and turbulent.
b) Adiabatic conditions are introduced on the nozzle's walls and substrate.
c) The working gas is air, and the gas is assumed to be inert.
d) The particles are assumed spherical, and the particle discrete phase is well diluted within the gas, so that the particles do not affect the flow.
e) Particle/particle interactions can occur while particles are rebounding inside the nozzle (collision between downstream and upstream particles).

The simulations were carried out using Reynolds Averaging Navier Stokes (RANS) equations to describe the turbulent flow field. In addition, the turbulent flow is modeled using the Realizable $k-\varepsilon$ model (Ref 15). Under the above assumptions, the governing equations for the flow field are described as:

- Instantaneous continuity equation

$$\frac{\partial \rho_g}{\partial t} + \nabla.\left(\rho_g \boldsymbol{u}_g\right) = 0 \tag{1}$$

where $\rho_g$ is the gas density, and $\boldsymbol{u}_g$ is the gas velocity. $\partial t$ and $\nabla$ designate time and spatial derivatives, respectively. $\nabla$ is defined as $(\partial x \quad \partial y \quad \partial z)^T$.

- Momentum equation

$$\frac{\partial}{\partial t}\left(\rho_g \boldsymbol{u}_g\right) + \nabla.\left(\rho_g \boldsymbol{u}_g \boldsymbol{u}_g\right) = -\nabla \mathrm{p} + \nabla.\left(\left(\mu_g + \mu_t\right)\left(\nabla \boldsymbol{u}_g + \nabla \boldsymbol{u}_g^{\mathrm{T}} - \frac{2}{3}\nabla.\left(\boldsymbol{u}_g \mathbb{I}\right)\right)\right) \tag{2}$$

where $\mu_g$ is the dynamic viscosity, $\mu_t$ is the turbulent viscosity, p is the pressure, and $\mathbb{I}$ is the identity tensor.

- Transport equations

$$\frac{\partial}{\partial t}\left(\rho_g k\right) + \nabla.\left(\rho_g k \boldsymbol{u}_g\right) = \nabla.\left(\left(\mu_g + \frac{\mu_t}{\sigma_k}\right)\nabla k\right) + G_k + G_b - \rho_g \varepsilon - Y_M \tag{3}$$

$$\frac{\partial}{\partial t}\left(\rho_g \varepsilon\right) + \nabla.\left(\rho_g \varepsilon \boldsymbol{u}_g\right) = \nabla.\left(\left(\mu_g + \frac{\mu_t}{\sigma_\varepsilon}\right)\nabla \varepsilon\right) + \rho_g C_1 S\varepsilon - \rho_g C_2 \frac{\varepsilon^2}{k + \sqrt{\nu\varepsilon}} + C_{1\varepsilon}\frac{\varepsilon}{k} C_{3\varepsilon} G_b \tag{4}$$

$$\mu_t = C_\mu \rho_g \frac{k^2}{\varepsilon} \tag{5}$$

with $k$ the turbulent kinetic energy and $\varepsilon$ the dissipation rate . $G_k$ and $G_b$ represents the generation of turbulence kinetic energy due to the mean velocity gradients and mean velocity, respectively; $Y_M$ represents the contribution of the fluctuating dilation in compressible turbulence to the overall dissipation rate calculated according to Sarkar and Balakrishanan (Ref 16). $\sigma_k = 1.0$ and $\sigma_\varepsilon = 1.2$ are the Prandtl numbers for $k$ and $\varepsilon$, respectively. $C_2, C_{1\varepsilon}, C_{3\varepsilon}$ are constants, $S$ is magnitude of strain rate, and $C_1$ is a variable depending on $k$, $\varepsilon$, and $S$. $C_\mu$ is a model parameter function of the mean strain and rotation rates, angular velocity, and the turbulence fields $k$ and $\varepsilon$. For more information, details can be found in (Ref 15).

To investigate the particles history inside the nozzle, the Discrete Phase toolbox of FLUENT was used. Particles of different diameters are injected on all the surface of the particle inlet. In the Lagrangian framework, the particle trajectories are solved by resolving the equation of motion on the particle:

$$m_p \frac{d\boldsymbol{u}_p}{dt} = \boldsymbol{F} \tag{6}$$

where $m_p$ is the particle mass, $\boldsymbol{u}_p$ is the particle velocity and $\boldsymbol{F}$ represents the overall forces acting on the particle. The forces considered in this study are the gravity $\boldsymbol{F}_{grav}$, the drag force $\boldsymbol{F}_{drag}$, the Saffman lift force $\boldsymbol{F}_{lift}$ , and the thermophoretic force $\boldsymbol{F}_{therm}$.

The gravity $\boldsymbol{F}_{grav}$ is given by:

$$\boldsymbol{F}_{grav} = \boldsymbol{g}\frac{\rho_p - \rho_g}{\rho_p} \tag{7}$$

where $\boldsymbol{g}$ is the gravity, and $\rho_p$ is the particle density.

The drag force per unit particle mass is given by:

$$\boldsymbol{F}_{drag} = F_D(\boldsymbol{u}_g - \boldsymbol{u}_p) \quad \text{with} \quad F_D = \frac{18\mu_g}{\rho_p d_p^2}\frac{C_D Re_p}{24} \tag{8}$$

where $\boldsymbol{u}_p$ is the particle velocity, $d_p$ is the particle diameter, $Re_p$ is the particle Reynolds number, and $C_D$ is the drag coefficient which follow the spherical Drag law (Ref 15,17):

$$C_D = a_1 + \frac{a_2}{Re_p} + \frac{a_3}{Re_p^2} \tag{9}$$

where $a_1, a_2$ and $a_3$ are dependent on the particle Reynolds number (Ref 17). In Appendix 1, the values of $a_1, a_2$ and $a_3$ parameters are recalled as mentioned in (Ref 17).

The Saffman lift force $\boldsymbol{F}_{lift}$ is used to represent the effect of shear forces on the particles. The lift force expression is a generalization of the Saffman expression (Ref 18,19) and is given by:

$$\boldsymbol{F}_{lift} = \frac{5.188\nu^{0.5}\rho_g}{\rho_p d_p}\frac{\mathbb{d}}{(\mathbb{d}:\mathbb{d})^{0.25}}\left(\boldsymbol{u}_g - \boldsymbol{u}_p\right) \tag{10}$$

where $\mathbb{d}$ is the deformation tensor defined as $\frac{1}{2}\left(\nabla\boldsymbol{u}_g + \left(\nabla\mathbf{u}_{\mathrm{g}}\right)^{\mathrm{T}}\right)$ and $\nu$ is the kinematic viscosity.

As the gas temperature is not uniform in the nozzle, particles will experience a force, known as thermophoretic force $\boldsymbol{F}_{therm}$, in the opposite direction of the thermal gradient:

$$\boldsymbol{F}_{therm} = -D_{T,p}\frac{1}{m_p T}\nabla T \tag{11}$$

where $m_p$ is the particle mass, $T$ is the absolute temperature, and $D_{T,p}$ is the thermophoretic coefficient given by (Ref 20):

$$D_{T,p} = \frac{6\pi d_p \mu_g^2 C_s(K + C_t K_n)}{\rho_g(1 + 3C_m K_n)(1 + 2K + 2C_t K_n)} \tag{12}$$

where $K_n$ is the Knudsen number, $K$ is the ratio of thermal conductivity between the gas and the particle, $C_s, C_t$ and $C_m$ are parameters equal to 1.17, 2.18 and 1.14, respectively.

During the cold spray process, particles are flying inside a pressurized heated gas. Due to the surrounded environment (hot gas), the particles will start to heat up. However, because of the low thermal conductivity of polymers, thermal equilibrium is never reached within the particles. Such phenomenon has been investigated by Bernard et al. (Ref 12) for polymer particles using a simple 2D axisymmetric model. Katanoda (Ref 21) and Raoelison (Ref 22) showed that, even though this phenomenon exists for metallic and ceramic particles, it remains negligeable in regards of the thermal stability of these material. In this paper, the particle thermal gradient will not be considered. It will be the aim of another paper. Thus, here, the comparison between the different particle sizes will be done through the particle average temperature $\langle T_p \rangle$ determined, at each step time, by the heat balance equation given by:

$$m_p c_{p_p}\frac{d\langle T_p\rangle}{dt} = hA_p\left(T_\infty - \langle T_p\rangle\right) \tag{13}$$

where $c_{p_p}$ is the particle's heat capacity, $A_p$ is the surface area of the particle, $h$ is the convective heat transfer coefficient, and $T_\infty$ is the local gas temperature.

### 2.3. Boundary conditions

The boundary conditions are schematically reproduced in Figure 2. For a standoff distance of 10 mm, Ravi et al. (Ref 5) determined the best spray conditions to be 0.4 MPa and 653 K for the inlet gas pressure and temperature, respectively. Adiabatic conditions are considered on the stainless-steel nozzle wall and aluminum substrate (no-slip wall). The substrate temperature is set at 300 K. Atmospheric pressure and room temperature are considered at the outlet and at the particle inlet. UHMWPE particles, initially at room temperature (300 K), are injected with a feeding rate of $7.5\times10^{-5}$ kg $s^{-1}$ on all the surface of the particle inlet with no initial velocity. The UHMWPE particles distribution is represented in Figure 3 and modelled using Rosin-Rammler distribution which assumes an exponential relationship between the particle diameter $d_p$ and the mass fraction of particles with diameter greater than $d_p$, $Y_{d_p}$ (Ref 15):

$$Y_{d_p} = \exp\left(-\left(\frac{d_p}{\langle d_p \rangle}\right)^n\right) \tag{14}$$

where $\langle d_p \rangle$ is the average particle size and $n$ is the size distribution parameter. The particle-tracking toolbox from Fluent is used to follow the particles' trajectory during its flight inside the nozzle. The material properties of the powder are presented in Table 1.

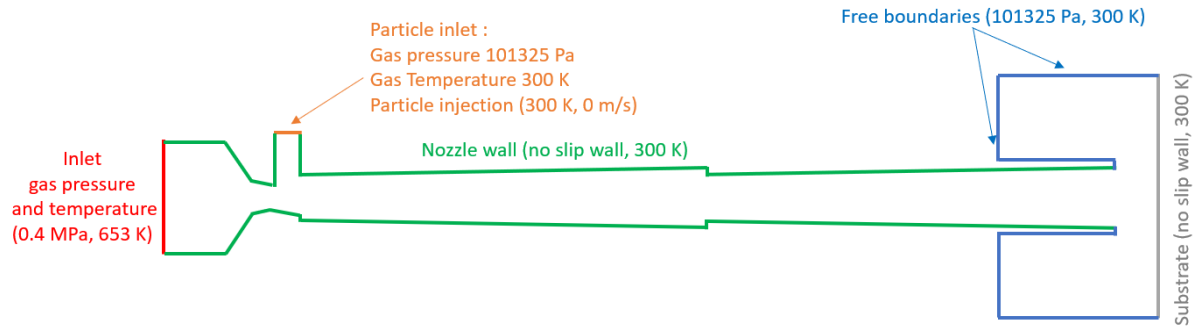


*Figure 2: Schematic representation of the boundary conditions.*

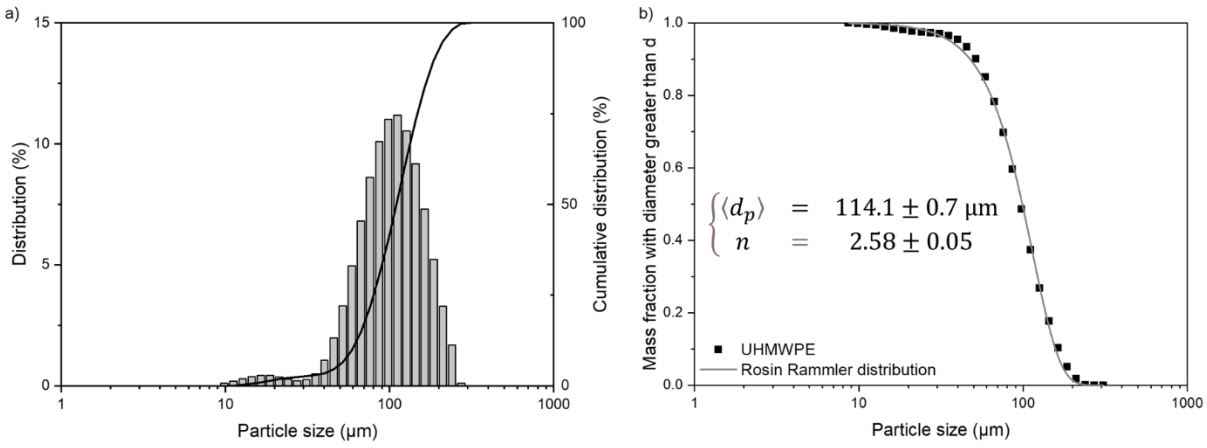


*Figure 3: a) UHMWPE particle distribution and b) Rosin Rammler distribution of the UHMWPE particles.*

*Table 1: Material properties of the polymer particles.*

| **Particle** |
|---|

| | |
|---|---|
| Material | UHMWPE |
| Density $\rho_p$ | 940 kg $m^{-3}$ |
| Specific heat $c_{p_p}$ | 2220 J $kg^{-1}$ $K^{-1}$ |
| Thermal conductivity $\Gamma_p$ | 0.41 W $m^{-1}$ $K^{-1}$ |
| Particle diameter $d_p$ | 10-272 µm |

## 3. Results and Discussion

### 3.1. Gas flow field

Generally, the gas flow field in cold-spray experiments is assumed to be axisymmetric. However, the presence of a powder feeder tends to delay the axisymmetry of the flow due to the income of cold and low pressurized air in the mainstream of the nozzle (see Figure 4). While the flow becomes axisymmetric early in the case of the 240 mm long nozzle, this one is delayed in the case of the 120 mm × 2 long divergent nozzle. Therefore, the flow becomes axisymmetric around a quarter of the total nozzle length in the case of the 120 mm × 2 long divergent nozzle. In addition, large vortexes are observed at the particle inlet entrance due to the mixing of cold and hot pressurized air, larger nozzle expansion and the reduction of the nozzle cross-section downstream. In addition, because of the presence of the supersonic flow just at the exit of the particle inlet, low temperature of the gas is observed (see Figure 5). This phenomenon, in addition to the reduction of the nozzle cross-section, leads to a very specific pattern for the streamline which will govern the particles' trajectory, at least, just after they enter the nozzle. In Figure 6, the evolution of the particle's trajectory is presented for both nozzles. In the case of the 240 mm long divergent nozzle, as the flow becomes axisymmetric early, the particles sprayed in all the nozzle diameter, and uniform temperature is observed for all the particles travelling in the same nozzle section. In the case of the 120 mm × 2 long divergent nozzle, from their entrance in the nozzle up to 90 mm in the nozzle (three-quarter of the first nozzle), all particles follow the same path, avoiding the low-pressure vortexes and following the mainstream line of the gas. Once the flow becomes axisymmetric, the particles start to spread in all the nozzle cross-section just before the intersection between the two nozzles. It leads to the rebound of some particles at the intersection between the two nozzles due to the 20% sharp reduction of the nozzle cross-section. In Figure 6, some hotter particles can be found in the first section of the nozzle. These particles have rebounded inside the nozzle and are going upstream. When rebounding at the intersection between the two nozzle sections, these particles are still subjected to the influence of the very hot gas surrounding them. Without the presence of the supersonic jet, and therefore, the decrease of gas temperature due to the gas expansion, the particles continue to heat up while rebounding inside the nozzle. Thus, not only their resident time in the nozzle increases, leading to increase their temperature, as observed in Figure 6, it also induces interactions with particles going downstream. Thus, not only particle/gas interaction exists but also particle/particle interaction can occur.

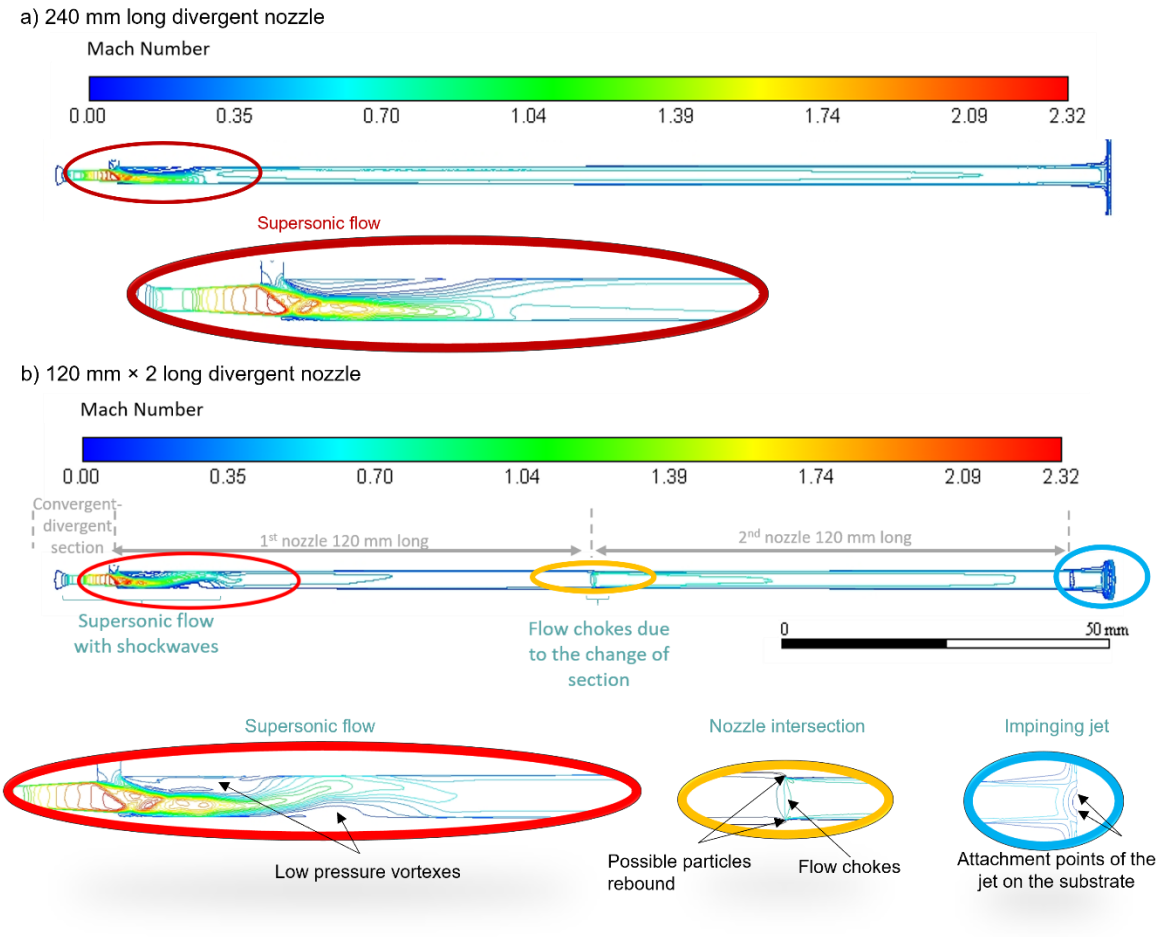


*Figure 4: Evolution of the Mach Number along the nozzle for a) 240 mm long divergent nozzle and b) 120 mm × 2 long divergent nozzle. For the 120 mm × 2 long divergent nozzle, two large vortexes are observed close to the particle inlet. In addition, at the intersection between the two nozzles, flow chokes due to the reduction of section.*

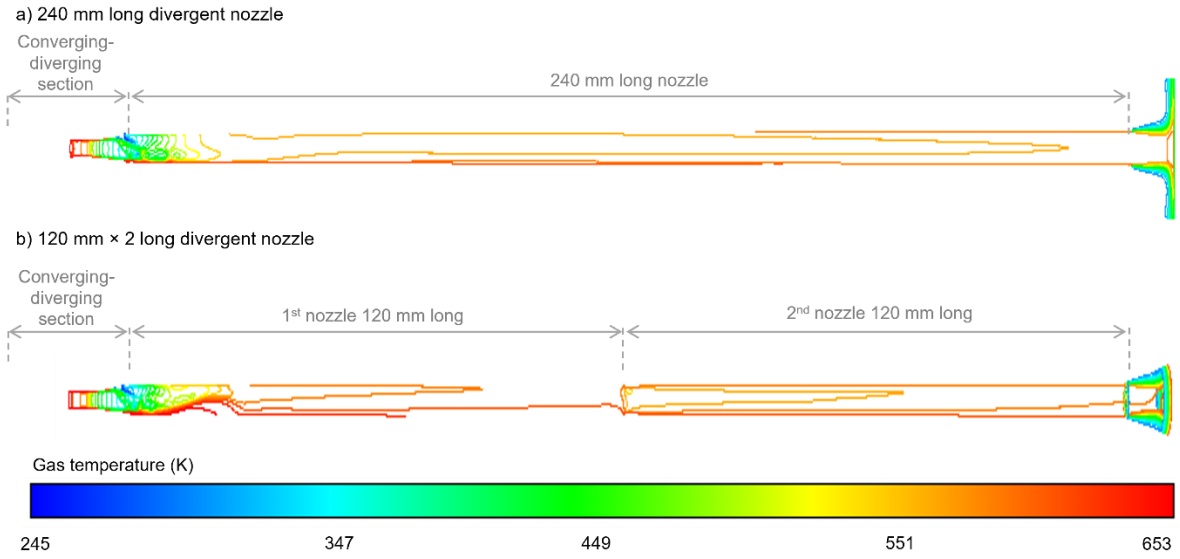


*Figure 5: Evolution of the gas temperature along the a) 240 mm long nozzle and b) 120 mm × 2 long nozzle. The supersonic flow is only located in the first half of the first nozzle section. At this location, the gas temperature is much colder than the rest of the nozzle due the combined effect of the supersonic flow and the gas at room temperature (300 K) entering from the particle inlet. At the intersection between the two nozzle sections, the gas temperature decreases due to the flow chokes. However, the gas temperature remains very hot (close to the gas inlet temperature (653 K)).*

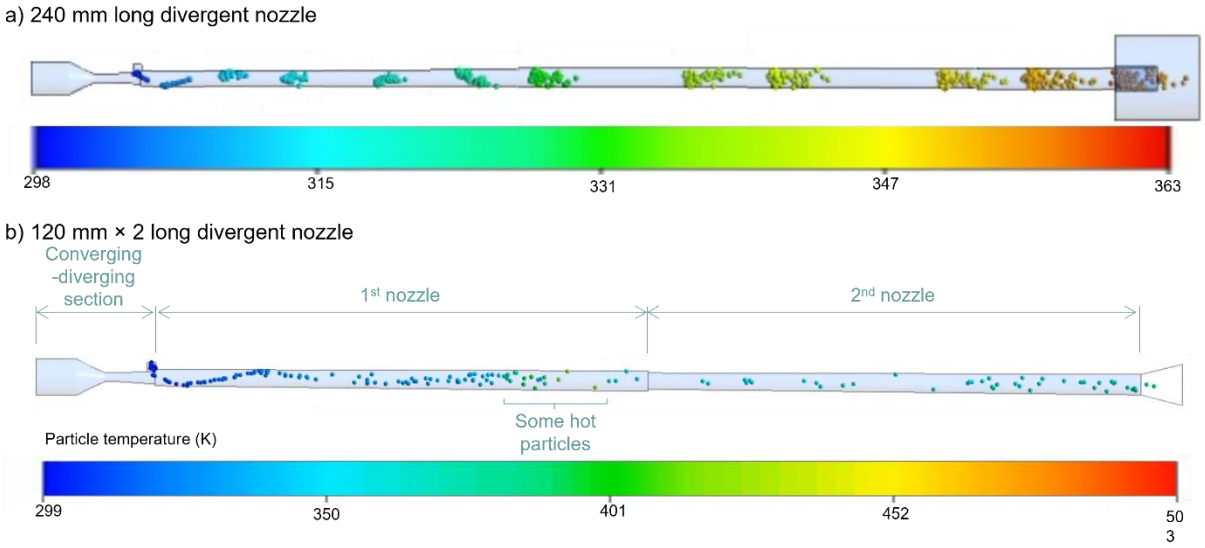


*Figure 6: Evolution of the particles' trajectories along the a) 240 mm long nozzle and b) 120 mm × 2 long nozzle. For the 120 mm × 2 long nozzle, at their entrance into the nozzle, all particles follow the same path. At the intersection between the two nozzle sections, some particles are rebounding inside the nozzle leading them to go upstream and reaching a higher temperature. All particles have a diameter of 60 µm.*

### 3.2. Probability of rebound

The probability of rebound of the particles inside the 120 mm ×2 long nozzle is represented in Figure 7 as a function of the particle diameter. For each diameter, more than 10,000 particles were sprayed on all the particle inlet surface. For particles with a diameter of less than 30 µm the probability of rebound inside the nozzle is around 5%, it highly increases up to 30% for 45 µm diameter particles, before stabilizing around 21%. That means that one fifth of the feedstock particles will rebound inside the nozzle. In addition, it is important to note that particles can rebound more than once inside the nozzle, and this highly depends on their diameter. Thus, some particles rebound up to 4 times inside the nozzle, leading to an important increase of their resident time, and, therefore, their temperature.

During its experiments, Ravi et al. (Ref 6) observed a very low deposition efficiency (lower than 1%) probably due to the combined effect of lack of mechanical interlocking and low particle temperature. According to the deposition window identified by Khalkhali et al. (Ref 8), the deposition of UHWMPE particles on UHWMPE substrate occurs when the particle temperature is above 80°C for a substrate temperature at 100°C. Thus, the larger the particle temperature, the more chance the particle can adhere on the substrate. Thus, rebounded particles, which spend more time inside the nozzle, and therefore have larger temperature than non-rebounded particles, will be expected to have more chance to adhere to the substrate and participate in the coating formation and build-up.

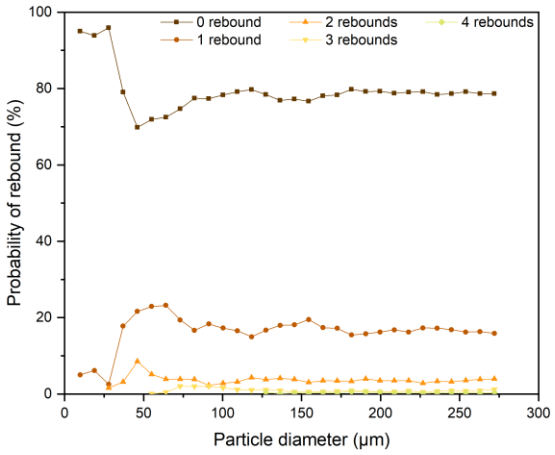


*Figure 7: Evolution of the probability of rebound in function of the particle size. The rebound occurs at the intersection between the two 120 mm-long nozzle sections due to a 20% sharp decrease of diameter. For each particle diameter, more than 10,000 particles were sprayed on all the surface of the particle inlet.*

For particles with a diameter greater than 30 µm, a sudden change in the rebound behavior inside the nozzle is observed (see Figure 7). For three different particles diameter, we investigated the forces balance in four characteristic locations inside the nozzle (in the supersonic flow, before and after the intersection between the two nozzle sections, and at the nozzle exit) The results are plotted in Figure 8. The gravity and thermophoretic forces are negligibly small compared with the Saffman lift force and drag force. When increasing the particle size, the contribution of the Saffman lift force increases. The bigger the particle, the more resistance they oppose to the flow field leading to a reduction of the contribution of the drag force. Therefore, by increasing the particle inertia, the particle velocity decreases. The particles becomes more influenced by the shear velocity and are more likely to disperse within the nozzle leading to higher rebound probability (Ref 23). On the contrary, particles with low inertia have high velocity and are carried by the flow field following a straight line (flow streamline). Therefore, they are less likely to get influenced by the shear velocity.

The ratio of drag force and Saffman lift force is highly dependent of the particle location inside the nozzle. If in the supersonic flow, after the intersection between the two nozzles, and at the nozzle exit, the force balance between drag and Saffman lift is relatively the same for a given particle size, it is not the case before the intersection between the two nozzle sections. At the end of the supersonic region, the Mach number decreases below 0.35 (see Figure 4). The influence of the Saffman lift force increases until 25% for the larger particles but remains small (less than 5% for 10 µm particles). Thus, the 10 µm particles tend to stay in the main streamline of the flow field, while larger particles, carried by the Safffman lift force, tend to fly across the main flow, and therefore, rebound on the nozzle wall and at the intersection between the two nozzle sections.

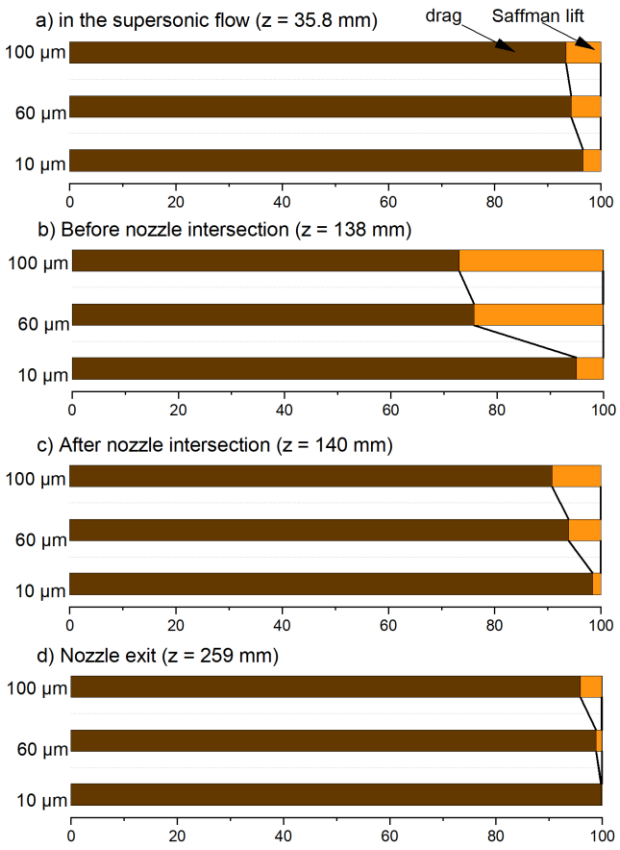


*Figure 8: Force balance acting on the particle at different locations of the 120 mm × 2 long nozzle: a) in the supersonic flow, b) before the intersection between the two nozzle sections, c) after the intersection between the two nozzle sections, and d) at the nozzle exit. Thermophoretic forces and gravity are neglectable in front of drag and Saffman lift forces.*

### 3.3. Particle in-flight behavior

Earlier, we emitted the assumption that the increase in temperature of the rebounded particles was due to the increase of their residence time inside the nozzle rather than their contact with the hot metallic nozzle surface due to their rebound at the intersection between the two nozzle sections. Proof was given through the evolution of the gas temperature (see Figure 5) inside the nozzle where the absence of supersonic flow in the rebounded area avoided the particles to cool down during their flight. An additional proof is provided here.

During their flight, the particles can rebound on the nozzle wall, and at the intersection between the two nozzle sections, leading to possible clocking of the nozzle (depending on the particle size). However, the contact time between the hot metallic surface and the particle being very short, in addition of polymer materials having a low thermal conductivity, the particle temperature increase is more likely due to the increase in the particle residence time inside the nozzle.

For three particle sizes (10, 60, and 100 µm), the particle velocity and temperature are plotted along the nozzle path (see Figure 9) and the two nozzle geometries are compared. If the particle impact velocity is lower for the 240 mm long nozzle compared to the 120 mm × 2 long nozzle, the particle temperature is roughly the same in absence of rebound at the intersection between the two nozzles. In particular, at the intersection between the two nozzle sections, either a second acceleration (non-rebounded particles) or a drop (rebounded particles) of the particle velocity is observed. In terms of particle temperature, the rebound is characterized by a significant increase in the particle temperature regardless the particle size.

According to Khalkhali and Rosthein (Ref 8), UHMWPE deposition over UHWMPE substrate (heated at 100°C) is possible for 20 µm having a temperature larger than 80°C and an impact velocity larger than 300 m $s^{-1}$. Thus, the presence of a step inside the nozzle allows increasing the particle velocity (for un-rebounded particles). In addition, by increasing the particle temperature, the particle velocity can be reduced, and the particle deposition still be observed. Therefore, it seems that the particle rebound inside the nozzle can only bring advantages in terms of particle temperature and velocity to achieve particle deposition on the substrate. However, as the deposition efficiency of UHMWPE particle on aluminum substrate remains substantially very low, it is necessary to think about other solutions or combination of solutions to increase the efficiency such as (i) increasing the substrate roughness by laser texturing or deposition of a metallic bond coat (Ref 11,24) to enhance mechanical interlocking, (ii) adding nanoceramics particles to the feedstock (Ref 2,5,10,25) to encourage chemical interlocking by the generation of Van der Walls bonds for example, and (iii) increasing the substrate temperature (Ref 7,8) to allows melting and co-crystallization of the polymeric chains.

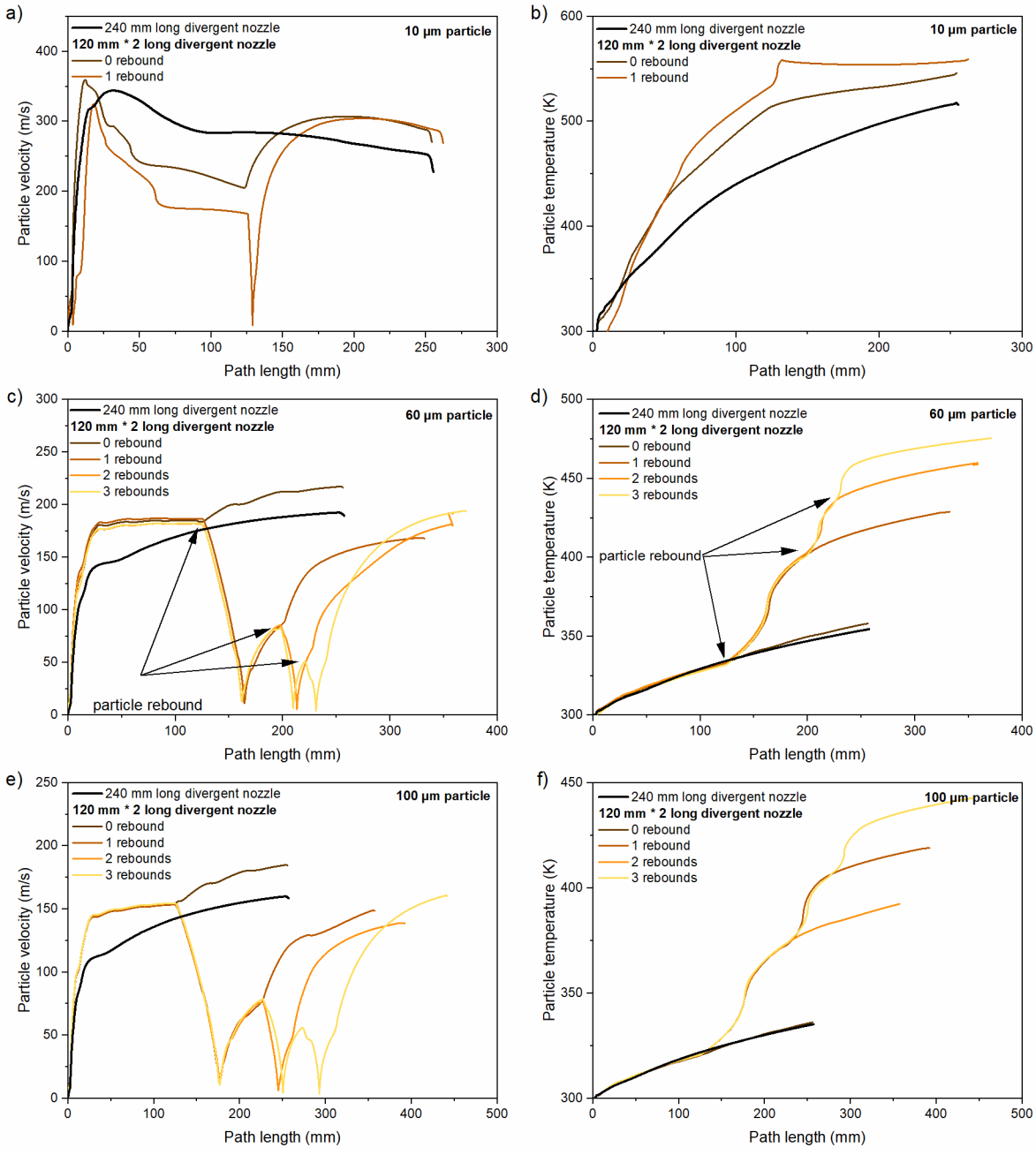

*Figure 9: Evolution of the particle velocity and temperature along the nozzle path for a,b) 10 µm particles, c,d) 60 µm particles, and e,f) 100 µm particles in function of the number of rebound. Comparison of the particle thermomechanical history between the 240 mm long divergent nozzle and the 120 mm × 2 long divergent nozzles.*

### 3.4. Particle behavior at the impact

The average temperature of the rebounded particles highly increases due to longer residence time inside the nozzle as shown in Figure 10a. While for the smallest particles (10 µm), the temperature difference between rebounded and un-rebounded particles remains negligeable, it is not the case for larger particles. Therefore, it can reasonably be assumed that the 10 µm particles exhibit a homogeneous temperature when reaching the substrate, while the thermal gradient induced by the process in all other particle sizes is significant enough to induce a gradient of material properties prior to the impact.

Considering that the initial degradation temperature of UHMWPE powder is around 515 K (Ref 26), the smallest particles start to decompose in the nozzle, which make them unfitted to be used with a long nozzle. The particles with a diameter between 15 and 30 µm and some rebounded particles with a larger diameter experience melting in the nozzle (melting temperature of native UHMWPE particles is around 415 K (Ref 5)). This can have two consequences: (i) possible clogging of the nozzle, (ii) better fluidity of the polymer particles which enhances entanglements between the neighboring particles upon impact inducing co-crystallization (Ref 27), and therefore, helping to build-up the coating.

The particle velocity as a function of their diameter is plotted in Figure 10b for different number of rebounds inside the nozzle. It is evident that the particle velocity decreases while increasing the particle size due to higher resistance of the particle to the flow. Once the particles rebound, their impact velocity drops by approximatively 25 m $s^{-1}$. This is due to the absence of supersonic flow in the particle trajectory after rebound. Thus, the rebounded particles do not experience the high velocity increase that they first experienced when they entered the nozzle. Only the second acceleration due to the reduction of the nozzle diameter allows to increase the particle velocity. However, this one is not enough for a particle having bounced to reach the same speed as a particle having not bounced. Thus, the particle velocity is independent of the number of times the particle rebounds inside the nozzle. Just by measuring the particle size and velocity at the nozzle exit, we can deduce that the particle has bounced inside the nozzle or not, and also whether the additional increase in particle temperature results from the longer resident time of the particle inside the nozzle.

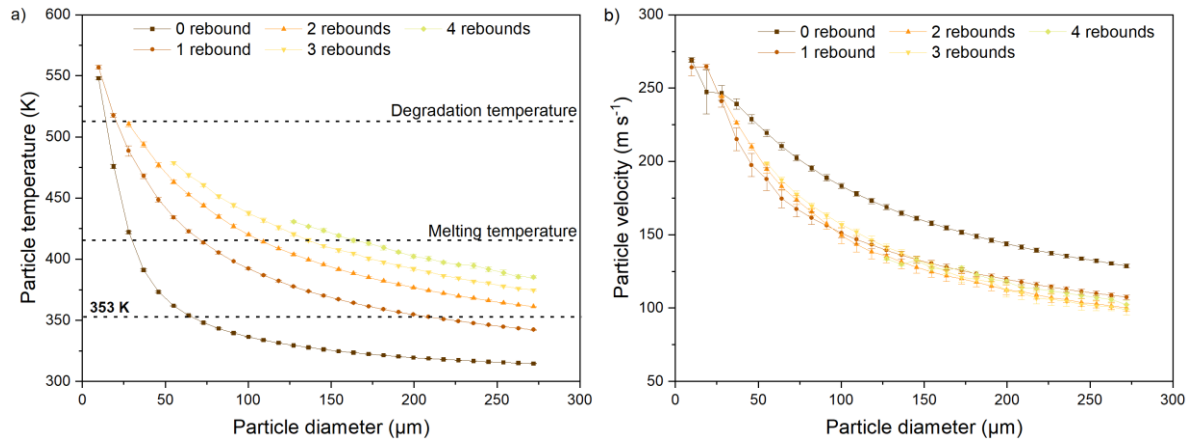


*Figure 10: Evolution of the a) particle temperature and b) particle velocity in function of the particle diameter and the number of times the particle rebound inside the nozzle. The particles are initially at 300 K. The melting temperature of native UHMWPE is at 415 K (Ref 5). The initial degradation temperature of UHWMPE powder is around 515 K (Ref 26).*

In Figure 11, the particle velocity is plotted as a function of the particle temperature for different number of rebound and particle diameter. Khalkhali et al.(Ref 8) investigated the deposition window of UHMWPE over UHMWPE while the substrate was heated at 373 K. The deposition window of 20±7 µm particle diameter requires a particle temperature above 353 K and a particle velocity of at least 300 m $s^{-1}$. If such temperature is reached for non-rebound particles with a diameter lower than 75 µm and for all rebounded particles, the particle velocity remains lower than 300 m $s^{-1}$ in all the cases. However, it is to be expected that the impact velocity allowing deposition decreases when the particle temperature increases. Therefore, it is more likely that even with low impact velocity, the particle with temperature close to the melting temperature, or even above, if not clogging the nozzle, will participate in the coating build-up. However, the question remains for the polymer coating formation, especially UHMWPE in this study, on a metallic substrate. An assumption will be that heating up the substrate to a temperature close to the polymer melting temperature, allowing the movement of polymeric chains, induces strong adhesion between the first layer and the substrate.

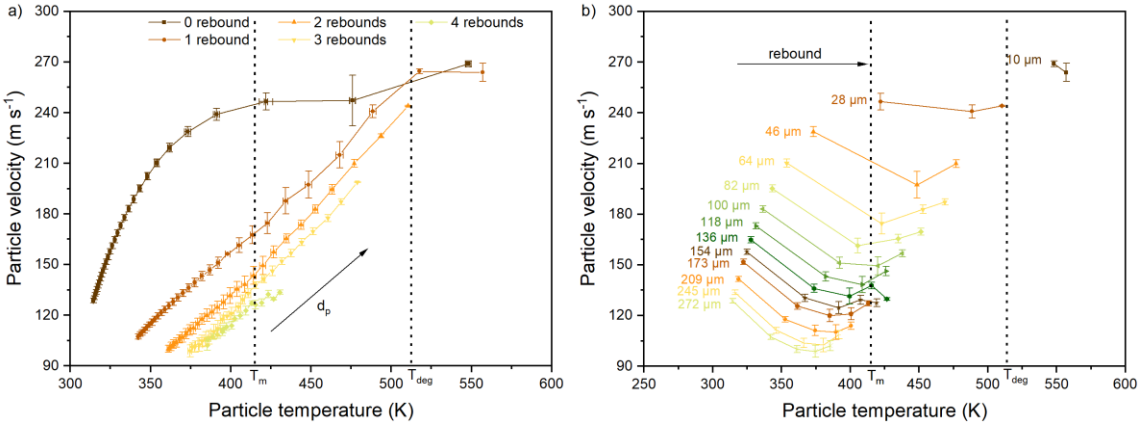


*Figure 11: Evolution of the particle velocity as a function of the particle temperature for a) and b) different particle diameter and different particle bounces.*

### 3.5. Particle distribution on the substrate

The particle distribution on the substrate for different particle sizes is plotted in Figure 12 for the 240 mm long divergent nozzle and in Figure 13 for the 120 mm × 2 long divergent nozzle. In the case of the 240 mm long divergent nozzle, the particles can still rebound on the nozzle wall, however, as there is no reduction of the nozzle's section, particles cannot go upstream unlike what it is observed for the 120 mm × 2 long divergent nozzle. The differentiation between bounced particles (red) and non-bounced particles (black) is made on Figure 13. For both nozzles, it can be observed that the deposition behavior of 10 µm diameter particles is ω-shaped. However, the area of deposition is larger for the 240 mm long divergent nozzle. For other particle diameters, the repartition of the particles on the substrate is more homogeneous. For both nozzles, more particles are sprayed on the center of the spray area. However, for the 120 mm × 2 long divergent nozzle, the particle density at the center is more important due to the particle rebound. In addition, it appears that the *y*-direction is a privileged axis of deposition. As the particle trajectory is modified by the particle bouncing, the distribution behavior of the rebounded particle on the substrate has no reason to be identical to the one of the non-rebounded particles. Thus, it can be observed in Figure 13, a large number of rebounded particles impacting in the center of the spray area leading to higher particle temperature at this particular location. In addition, for particles with diameter between 30 and 60 µm, concentrated circles of rebounded particles can be observed between 1 and 2 mm from the spray center. For larger particle size, the rebounded particles are mainly impacting at the center of the spray area, with few particles, in comparison, impacting on the outskirt of the spray area. It is also interesting to note that very few

particles impact outside of 5 mm spray area (corresponding to the nozzle exit diameter). Only the biggest particle with lower velocity and temperature can be deposited in that region. Thus, it seems, that these particles are carried by the impinging jet in front of the substrate, rather than flying straight to the substrate. However, increasing their temperature allows them to penetrate through this physical barrier.

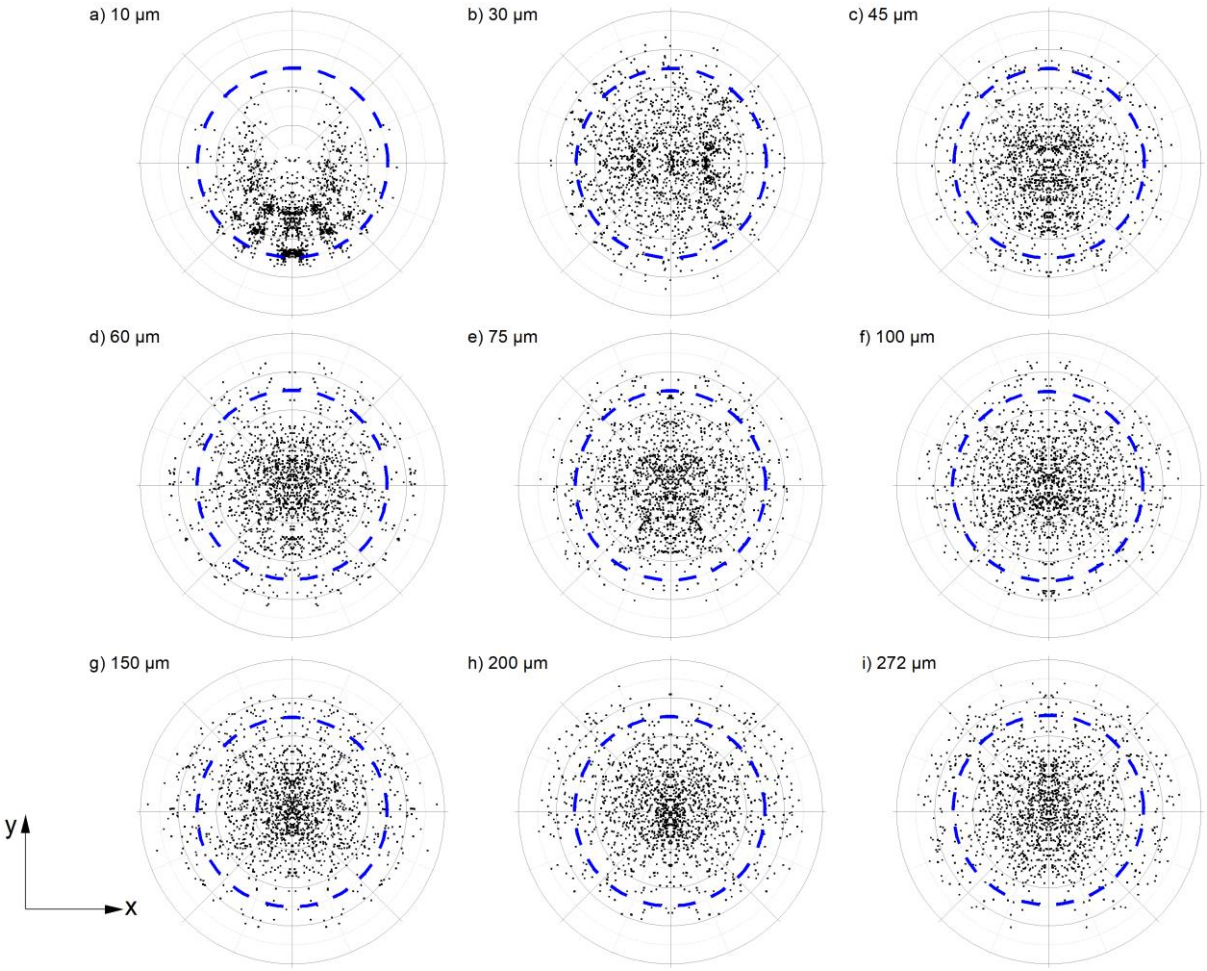


*Figure 12: Repartition on the substrate of the particles sprayed with the 240 mm long divergent nozzle for different particle sizes. The diameter of the blue dashed circle is equal to 5 mm, i.e., the nozzle exit diameter.*

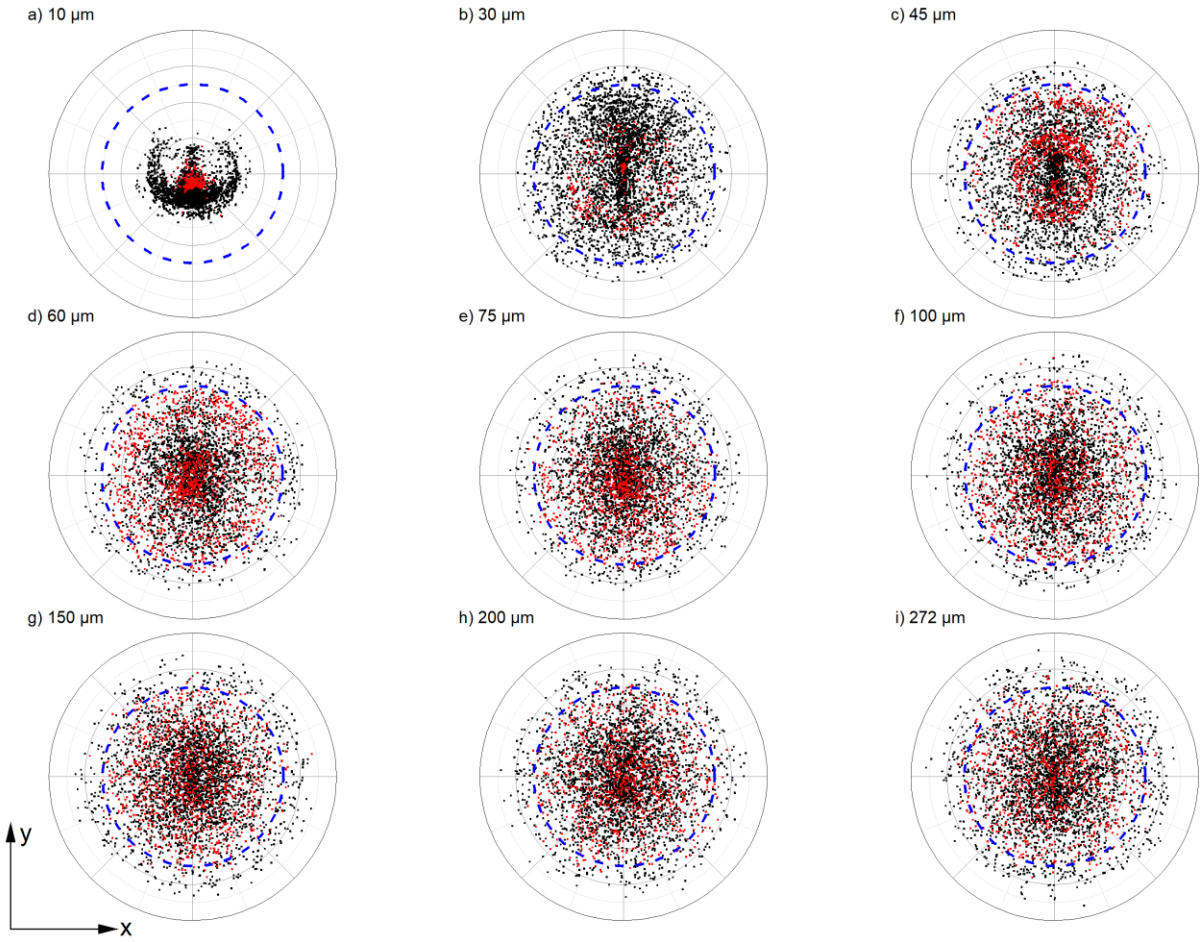


*Figure 13: Repartition on the substrate of the rebounded particles (in red) and non-rebounded particles (in black) sprayed with the 120 mm × 2 long divergent nozzle for different particle sizes. The diameter of the blue dashed circle is equal to 5 mm, i.e., the nozzle exit diameter.*

Figure 13 shows the distribution of the number of particles on the substrate as a function of the particle size. In Figure 14a, for better understanding, groups of three particle's diameters were considered. Each group of particles regroups around 38,000 particles. The particle distribution on the substrate follows a Gaussian function distribution centered at 0 (center of the spray area). For a given position on the substrate, the particle size distribution is roughly the same, except for particles with a diameter lower than 28 µm. For them (diameter < 28 µm), more small particles impact the center of the spray area (in comparison with other particle diameters). Therefore, small particles have enough kinetic energy to fly straight to the substrate. Fewer particles are reaching the substrate outskirt (outside of the nozzle exit projected surface area on the substrate). Therefore, if the spraying is always done at the same locations, a very rough coating in a shape of mountains and valleys, is expected. To avoid this and obtain a smoother coated surface, one solution would be to move the spray location slightly between each pass.

The normalized particle size distribution per size range is plotted in Figure 14b. Between 0 and 0.4 mm, the same amount of particles with a diameter lower than 28 µm is observed. After that point, the number of small particles decreases drastically. For other particle sizes, the particle density on the substrate is continuously decreasing to reach 0 at the outskirt of the spray area. The particle density plot is similar to a Gaussian function. However, it should be noted that the distribution appears wider than usual Gaussian function. It is especially true when increasing the particle size. This can be explained partially by the following. After bouncing inside the nozzle, the particle velocity decreases, and they become unable to fly straight to the substrate. Therefore, larger number of rebounded

particles is observed at the boundary around the attachment area of the impinging jet on the substrate (see Figure 4c and Figure 13c), which results in a second peak on the substrate between 1 and 2 mm (see Figure 14a).

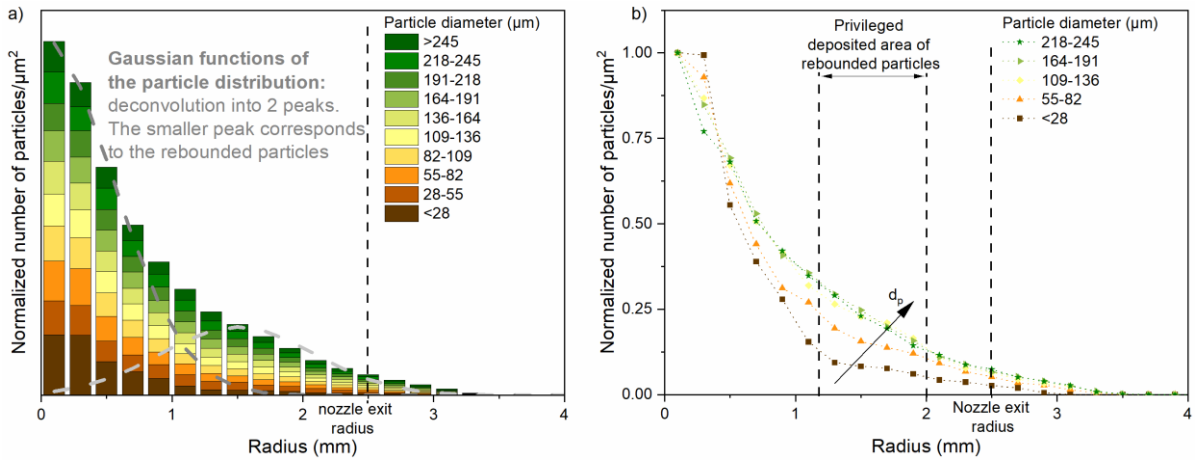


*Figure 14: Surface density of particles on the substrate considering the particle size. a) Particles distribution (all sized included). Each group of particle sizes have roughly the same number of particles (around 38,000 particles). b) Particle distribution per size range.*

## 4. Conclusion

This study focuses on the irregularities of the nozzle inner shape on the in-flight particle thermomechanical history during cold spray process using CFD simulations. For the realization of polymer coatings by cold spray, a long nozzle is beneficial to increase the particle temperature while limiting the particle velocity. However, they are not easy to manufacture in a single block. A solution is to attach (at least) two divergent nozzles, therefore modifying the inner shape of the nozzle, such as a sharp diameter changes, to induce turbulent flows. In our example, at the intersection between the two nozzle sections, the flow will choke leading to a second acceleration of the particles in the middle of the nozzle (the first acceleration occurs at the particles entrance in the nozzle).

Because of the reduction of cross-section at the intersection between the two nozzle sections, particles can rebound on the nozzle wall and bounce back upstream. Such phenomenon is possible thanks to the large influence of the Saffman lift force on the particles with a diameter larger than 30 µm near the intersection area. On the contrary, particles with a diameter lower than 30 µm have less tendency to rebound due to the predominance of the drag force and smaller inertia during all their flight inside the nozzle. By rebounding inside the nozzle, the particles residence time increases, and therefore, their temperature as well, while the particle velocity slightly decreases. In addition, the deposition behavior of the rebounded particles on the substrate exhibits a circular shape within a radius of 1.5 mm from the central axis. This corresponds to the attachment location of the impinging jet on the substrate.

In the polymer coating by cold spray process, only particles with enough temperature, but low velocity, can participate in the coating formation and build-up. Thus, the chance of deposition seems higher for rebounded particles than the non-rebounded one. A plausible solution to increase the deposition efficiency of polymer particle to adhere on the substrate will be to set the substrate temperature close to the melting temperature of the polymer to increase the particle temperature upon impact.

The particle rebound inside the nozzle can concern up to 30% of the particles (depending on the particle diameter for the material investigated) and increase considerably the particle temperature which will be beneficial to achieve the coating formation. However, in absence of rebound, the

particles behave the same as they will in a conventional nozzle (no decrease of the nozzle cross-section).

**Appendix 1**

The drag coefficient, $C_D$, is function of the particle Reynolds number $Re_p$. In this study, it is modelled using the spherical drag law equation as defined in eq. (9). The evolution of the $a_1$, $a_2$ and $a_3$ parameters in function of the particle Reynolds number is given in

*Table 2: Evolution of the $a_1$, $a_2$ and $a_3$ parameters (see eq. (9) in function of the particle Reynolds number used to calculate the drag coefficient.*

| $Re_p$ | $a_1$ | $a_2$ | $a_3$ |
|---|---|---|---|
| $Re_p < 0.1$ | 0 | 24 | 0 |
| $0.1 < Re_p < 1$ | 3.69 | 22.73 | 0.0903 |
| $1 < Re_p < 10$ | 1.222 | 29.1667 | -3.8889 |
| $10 < Re_p < 100$ | 0.6167 | 46.5 | -116.67 |
| $100 < Re_p < 1000$ | 0.3644 | 98.33 | -2778 |
| $1000 < Re_p < 5000$ | 0.357 | 148.62 | $-4.75\times10^4$ |
| $5000 < Re_p < 10000$ | 0.46 | -490.546 | $57.87\times10^4$ |
| $10000 < Re_p < 50000$ | 0.5191 | -1662.5 | $5.4167\times10^6$ |

**Acknowledgments**

The authors would like to acknowledge the Institute of Fluid Science at Tohoku University, which supported this research through grant J19Ly01 and J20Ly03 under the label of the LyC Collaborative Research Project.

**References**

1. A. Papyrin, V. Kosarev, S. Klinkov, A. Alkhimov, and V.M. Fomin, “Cold Spray Technology,” Elsevier, 2006.
2. K. Ravi, W.L. Sulen, C. Bernard, Y. Ichikawa, and K. Ogawa, Fabrication of Micro-/Nano-Structured Super-Hydrophobic Fluorinated Polymer Coatings by Cold-Spray, *Surface and Coatings Technology*, 2019, **373**, p 17–24.
3. W. Lock Sulen, K. Ravi, C. Bernard, Y. Ichikawa, and K. Ogawa, Deposition Mechanism Analysis of Cold-Sprayed Fluoropolymer Coatings and Its Wettability Evaluation, *Journal of Thermal Spray Technology*, 2020, **29**(7), p 1643–1659.
4. A.S. Alhulaifi, G.A. Buck, and W.J. Arbegast, Numerical and Experimental Investigation of Cold Spray Gas Dynamic Effects for Polymer Coating, *Journal of Thermal Spray Technology*, 2012, **21**(5), p 852–862.
5. K. Ravi, Y. Ichikawa, T. Deplancke, K. Ogawa, O. Lame, and J.-Y. Cavaille, Development of Ultra-High Molecular Weight Polyethylene (UHMWPE) Coating by Cold Spray Technique, *Journal of Thermal Spray Technology*, 2015, **24**(6), p 1015–1025.
6. K. Ravi, Y. Ichikawa, K. Ogawa, T. Deplancke, O. Lame, and J.-Y. Cavaille, Mechanistic Study and Characterization of Cold-Sprayed Ultra-High Molecular Weight Polyethylene-Nano-Ceramic Composite Coating, *Journal of Thermal Spray Technology*, 2016, **25**(1), p 160–169.
7. T.B. Bush, Z. Khalkhali, V. Champagne, D.P. Schmidt, and J.P. Rothstein, Optimization of Cold Spray Deposition of High-Density Polyethylene Powders, *Journal of Thermal Spray Technology*, 2017, **26**(7), p 1548–1564.

8. Z. Khalkhali and J.P. Rothstein, Characterization of the Cold Spray Deposition of a Wide Variety of Polymeric Powders, *Surface and Coatings Technology*, 2020, **383**, p 125251.
9. Y. Xu and I.M. Hutchings, Cold Spray Deposition of Thermoplastic Powder, *Surface and Coatings Technology*, 2006, **201**(6), p 3044–3050.
10. W.L. Sulen, K. Ravi, C. Bernard, N. Mary, Y. Ichikawa, and K. Ogawa, Effects of Nano-Ceramic Particle Addition for Cold Sprayed Fluoropolymer Coatings, *Key Engineering Materials*, 2019, **813**, p 141–146.
11. W. Lock Sulen, C. Bernard, Y. Ichikawa, K. Ogawa, J. Ishizaki, and S. Onodera, "Effect of Laser Texturing on Cold Sprayed Fluorinated Polymer Coatings," *Proceedings of the 112th National Meeting of Japan Thermal Spray Society*, 2020.
12. C. Bernard, H. Takana, G. Diguet, K. Ravi, O. Lame, K. Ogawa, and J.-Y. Cavaillé, Thermal Gradient of in-Flight Polymer Particles during Cold Spraying, *Journal of Materials Processing Technology*, 2020, **286**, p 116805.
13. H. Takana, K. Ogawa, T. Shoji, and H. Nishiyama, Computational Simulation of Cold Spray Process Assisted by Electrostatic Force, *Powder Technology*, 2008, **185**(2), p 116–123.
14. H. Takana, K. Ogawa, T. Shoji, and H. Nishiyama, Computational Simulation on Performance Enhancement of Cold Gas Dynamic Spray Processes with Electrostatic Assist, *Journal of Fluids Engineering*, 2008, **130**(8), p 081701.
15. ANSYS, Inc., "Ansys Fluent Tutorial Guide," (Canonsburg, PA, USA), ANSYS, Inc., 2017.
16. S. Sarkar and B. Lakshmanan, Application of a Reynolds Stress Turbulence Model to the Compressible Shear Layer, *AIAA journal*, 1991, **29**(5), p 743–749.
17. S. Morsi and A. Alexander, An Investigation of Particle Trajectories in Two-Phase Flow Systems, *Journal of Fluid mechanics*, 1972, **55**(2), p 193–208.
18. P. Saffman, The Lift on a Small Sphere in a Slow Shear Flow, *Journal of fluid mechanics*, 1965, **22**(2), p 385–400.
19. A. Li and G. Ahmadi, Dispersion and Deposition of Spherical Particles from Point Sources in a Turbulent Channel Flow, *Aerosol science and technology*, 1992, **16**(4), p 209–226.
20. L. Talbot, R.K. Cheng, R.W. Schefer, and D.R. Willis, Thermophoresis of Particles in a Heated Boundary Layer, *Journal of Fluid Mechanics*, 1980, **101**(4), p 737–758.
21. H. Katanoda, Numerical Simulation of Temperature Uniformity within Solid Particles in Cold Spray, *Journal of Solid Mechanics and Materials Engineering*, 2008, **2**(1), p 58–69.
22. R.N. Raoelison, M.R. Guéchi, and E. Padayodi, In-Flight Temperature of Solid Micrometric Powders during Cold Spray Additive Manufacturing, *International Journal of Thermal Sciences*, 2020, **157**, p 106422.
23. S.K. Jha, Effect of Particle Inertia on the Transport of Particle-Laden Open Channel Flow, *European Journal of Mechanics - B/Fluids*, 2017, **62**, p 32–41.
24. W. Lock Sulen, H. Saito, C. Bernard, Y. Ichikawa, and K. Ogawa, "High Deposition Efficiency of Super-Hydrophobic Fluoropolymer Coating on Metallic Substrate by Cold-Spray Process," *Proceedings of ITSC2021*, (Quebec City, Canada), ongoing.
25. K. Ravi, T. Deplancke, K. Ogawa, J.-Y. Cavaillé, and O. Lame, Understanding Deposition Mechanism in Cold Sprayed Ultra High Molecular Weight Polyethylene Coatings on Metals by Isolated Particle Deposition Method, *Additive Manufacturing*, 2018, **21**, p 191–200.
26. E. Rudnik and Z. Dobkowski, Thermal Degradation of UHMWPE, *Journal of thermal analysis*, 1997, **49**(1), p 471–475.
27. T. Deplancke, O. Lame, F. Rousset, I. Aguili, R. Seguela, and G. Vigier, Diffusion versus Cocrystallization of Very Long Polymer Chains at Interfaces: Experimental Study of Sintering of UHMWPE Nascent Powder, *Macromolecules*, 2014, **47**(1), p 197–207.